



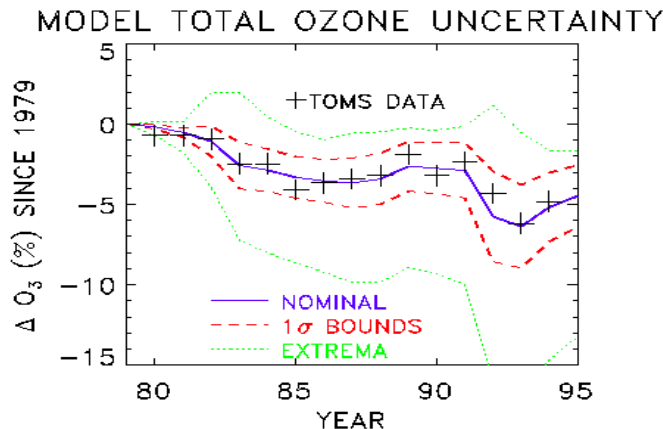
6. Highlights of Laboratory for Atmospheres Activities in 1998

Scientists in the Laboratory for Atmospheres have contributed directly to the advancement of Earth and space science by publishing 186 articles in refereed journals during the past year. A list of these publications appears in Appendix 7. Laboratory scientists have also presented talks and written articles for public and professional audiences. Other publications by Laboratory scientists include NASA Technical Memoranda, technical books and book chapters, and position papers related to national and international scientific policy issues listed in Appendix 6. In this section, we present a few examples selected from work completed or nearly completed during 1998. The selection process was somewhat subjective. Only time will tell the ultimate impact that these contributions will have. All the highlights listed below are the achievements not only of civil servants and non-government personnel who work in the Laboratory, but also of many other colleagues at GSFC, at NASA Headquarters, and at other NASA centers, most notably Ames Research Center, Langley Research Center, the Jet Propulsion Laboratory, and Marshall Space Flight Center. Private companies, other government laboratories, and universities in the United States and abroad have all made significant contributions to the work done in the Laboratory.

Ozone and Trace Gas Studies

A Monte Carlo Uncertainty Analysis of Ozone Trend Predictions in a Two-Dimensional Model

We've used a Monte Carlo technique to quantify, for the first time, uncertainty in a two-dimensional (2D) model of stratospheric photochemistry. The Goddard Space Flight Center 2D model of stratospheric photochemistry and dynamics requires parameters such as reaction rates and photolysis cross sections to be input before making specific predictions about the atmosphere. Each of these parameters is a measured quantity and is therefore uncertain to some degree. Consequently, some uncertainty occurs in the model predictions, even if the model itself is perfect. Knowing the amount of uncertainty in a model prediction will help us determine the significance of differences between the prediction and an observation. If the difference is small compared to the uncertainty, then the difference could easily be due to errors in the input parameters. If the difference is large compared to the uncertainty, then the model formulation itself is probably incorrect and needs to be examined. We used a Monte Carlo technique to quantify the input parameter uncertainty in model predictions of total ozone changes due to increases in stratospheric chlorine concentrations between 1979 and 1995. We have compared the uncertainty to discrepancies between the model predictions and observed changes over the same period, using TOMS version 7 total ozone observations. Figure 2 compares TOMS version 7 total ozone observations to model-calculated total ozone averaged annually and globally between 1979 and 1995. The crosses show the TOMS data, and the solid line shows the model result. The dashed lines indicate the $\pm 1 \sigma$ variation calculated from the Monte Carlo uncertainty analysis. Figure 2 shows that the model/measurement discrepancy is smaller than the uncertainty in the model result due to the input parameters. We therefore discern no significant difference between the observation and the model prediction. We have also used a statistical trend analysis of the model-calculated and observed trends to confirm this result. The linear trend in the model total ozone, averaged globally and annually, differs from the observed trend by 34%, which is smaller than the calculated 46% model uncertainty resulting from the input parameters. We find model/measurement discrepancies in the meridional gradients and seasonal variability of the ozone trends that are much larger than the model uncertainty due to the input parameters. These differences unambiguously indicate problems in model formulation and provide a measure of model performance that can be used in attempts to improve the model.



Uncertainty in the GSFC 2D Model 1979 – 1995 total ozone time series compared to TOMS data. Solid line: Percent change in the GSFC 2D model annually and globally averaged total ozone. Dashed line: $\pm 1\sigma$ uncertainty due to input reaction rates and photolysis cross-sections calculated for first time in a 2D model using a Monte Carlo uncertainty analysis. Crosses: TOMS annually and globally averaged total ozone. The model agrees with measurements within the model uncertainty.

Figure 2. Uncertainty in the GSFC 2D Model 1979-1995 total ozone time series compared to TOMS data. Solid line: Percent change in the GSFC 2D model annually and globally averaged total ozone. Dashed line: $\pm 1\sigma$ uncertainty due to input reaction rates and photolysis cross-sections calculated for first time in 2D model using a Monte Carlo uncertainty analysis. Crosses: TOMS annually and globally averaged total ozone. The model agrees with measurements within the model uncertainty.

Considine, D. B., R. S. Stolarski, S. M. Hollandsworth, C. H. Jackman, and E. L. Fleming, 1998: A Monte Carlo uncertainty analysis of ozone trend predictions in a two-dimensional model, *J. Geophys. Res.* **104**, 1749-1765.

Effects of 1997-1998 El Niño on Tropospheric Ozone and Water Vapor How did the 1997-1998 El Niño affect tropospheric column ozone and tropospheric water vapor? We've addressed this question by examining data from the TOMS on Earth Probe and the Microwave Limb Scanning instrument on the Upper Atmosphere Research Satellite. The 1997-1998 El Niño is one of the strongest El Niño Southern Oscillation (ENSO) events of the century. In magnitude, it resembles the 1982-83 episode. The 1997-1998 El Niño was characterized by an anomalous increase in SST across the eastern and central tropical Pacific Ocean. The major impact of the SST change has been the shift in the convection pattern from the western to the eastern Pacific, affecting the response of rain-producing cumulonimbus. As a result, we have seen a significant increase in rainfall over the eastern Pacific and a decrease over the western Pacific and Indonesia. The dryness in the Indonesian region has contributed to large-scale burning by uncontrolled wildfires in the tropical rainforests of Sumatra and Borneo. Our study shows that tropospheric column ozone decreased by 4-8 Dobson units (DU) in the eastern Pacific and increased by about 10-20 DU in the western Pacific. These changes arise largely from the eastward shift of the tropical convective activity as inferred from National Oceanic and Atmospheric Administration (NOAA) outgoing longwave radiation (OLR) data. The effect of this shift is also evident in the upper tropospheric water vapor mixing ratio, which varies inversely as ozone (O_3). These conclusions are qualitatively consistent with the changes in atmospheric circulation derived from zonal and vertical wind data obtained from the Goddard Earth Observing System data assimilation analyses. The changes in tropospheric column O_3 during the course of the 1997-1998 El Niño appear to arise from a combination of two phenomena: large-scale circulation processes associated with the shift in the tropical

convection pattern and surface/boundary layer processes associated with forest fires in the Indonesian region.

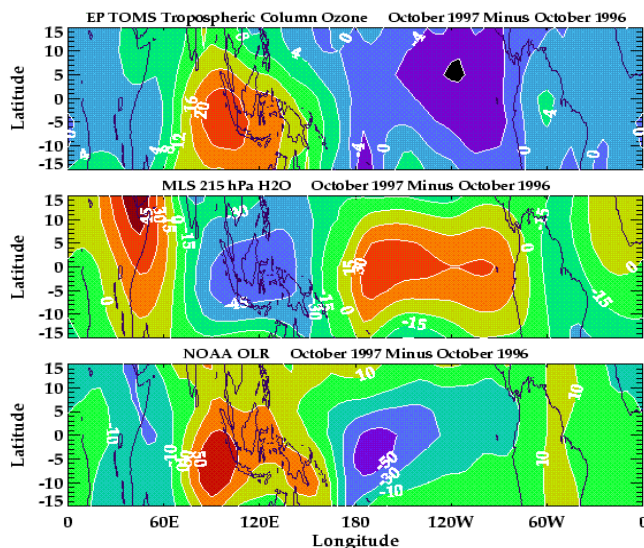


Figure 3. Tropical anomalies showing the effects of El Niño during October 1997. Anomalies were computed by subtracting October 1996 monthly-mean data from that of October 1997. From top to bottom, tropospheric column ozone (Dobson unit), H₂O volume mixing ratio (units parts per million by volume) at 215 hPa, and outgoing long wave radiation (OLR) flux (units W m⁻²).

Chandra, S., J. R. Ziemke, W. Min, and W. G. Read, Effects of 1997-1998 El Niño on Tropospheric Ozone and Water Vapor, 1998. *GRL Highlights*, **25**, 3867-3870.

Doubled CO₂ Effects on NO_y in a Coupled 2D Model Studies of the stratospheric impact of doubled CO₂ have focused on changes in temperature and ozone. Increased CO₂ is expected to cool the stratosphere, which will result in increases in upper stratospheric ozone through temperature-dependent loss rates. Less attention has been paid to changes in minor constituents that affect the ozone balance and that may provide additional feedbacks. Total reactive nitrogen NO_y = N + NO + NO₂ + NO₃ + 2xN₂O₅ + HNO₃ + ... is one of the most important minor constituents of the stratosphere. NO and NO₂ participate in a catalytic cycle of ozone destruction, and their contribution to the total ozone loss is significant throughout much of the stratosphere. Simulations using the GSFC 2D (latitude-height) interactive chemistry-radiation-dynamics model indicate that cooling in the upper stratosphere, calculated to result from doubling atmospheric CO₂, would lead to a net decrease in NO_y throughout the stratosphere due to the temperature dependence of kinetic rates. Doubling CO₂ increases stratospheric ozone, because the kinetic rates controlling O₃ loss are slower at temperatures lowered by CO₂ cooling. The decreases in NO_y, shown in Figure 4, also lead to a reduction in the loss of ozone because of the direct effect on the nitrogen catalytic cycles. Analyses of the model output show 10-15% decreases in the ozone loss rate due to the NO_y changes. This is significant when compared to the 25% decrease in the ozone loss rate due directly to the temperature changes. The figure shows the resulting increases in ozone, which are due to both the direct and the indirect effects of the temperature changes. These changes from CO₂ cooling and the importance of NO_y photochemical processes throughout the stratosphere point up the need to consider perturbations in constituents other than O₃ when

considering the interactions between stratospheric chemistry and climate.

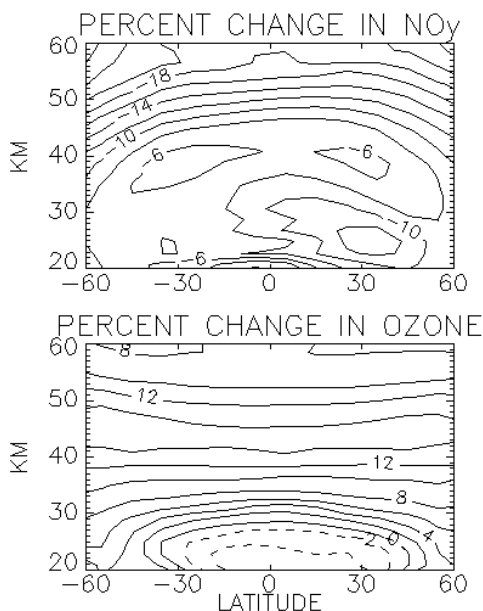


Figure 4. Percent changes in NO_y and ozone.

Rosenfield, J. E. and A. R. Douglass, 1998: Doubled CO₂ effects on NO_y in a coupled 2D model. *Geophys. Res. Lett.*, **25**, 4381-4384.

Remote Sensing of Clouds and Water Vapor

Evolution and Impact of Contrail Cirrus from Airborne Remote Sensing

Contrail cirrus is the special type of cirrus that forms as a result of aircraft emissions. Could contrail cirrus be a factor in climate change? We're attempting to answer this question using data from airborne remote sensing of clouds. The influence of contrail cirrus on climate depends on whether aircraft change the radiative forcing of the cirrus that would have occurred naturally without the aircraft influence. We determine the radiative forcing by observing cloud amount, distribution, and microphysics. As part of the SUCCESS, the NASA ER-2 aircraft was employed specifically for remote sensing of cirrus and contrail cirrus to address the question of contrail cirrus' effect on climate. We obtained microphysical analysis for cases of contrail cirrus that form in the same area as cirrus but have different maturity. To do so, we used multispectral thermal infrared radiance combined with lidar profiling. Figure 5 shows an example of the retrieved particle number density for old and new cirrus. In both cases, the inferred number of particles per distance along the flight track dimension of contrails was similar, close to 2.6 trillion per meter. However, while the average liquid water concentration of the two cases was similar, the total amount of water per distance along the flight line dimension was much greater for the older contrail. The results are consistent with a model of contrail evolution in which the effect of the jet exhaust is first to generate a dense concentration of small ice particles. When the particles mix with surrounding air, the total number of particles does not change but the particle number density becomes much less. The water vapor in excess of ice saturation condenses on the particles. This process leads to a constant characteristic value of ice-to-liquid water density for the contrail. The total water amount grows with the spreading and mixing of the contrail into the surrounding air. The evidence shows that aging contrails become similar to surrounding, naturally occurring cirrus in particle size and liquid

water content. The overall effect of contrail cirrus formation globally remains unknown.

Contrail Cirrus Evolution

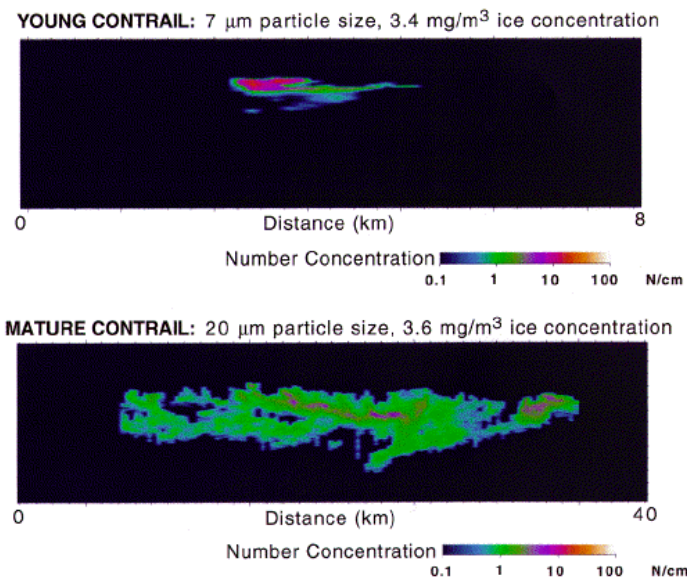


Figure 5. The top panel shows the cross section of a contrail observed shortly after formation and the bottom panel shows the cross section approximately an hour older. The calculated number density of particles is shown by the color scale. The number density of particles for the mature contrail is much less but the average ice/water concentration is the same.

Spinhirne, J. D., W. D. Hart, and D. P. Duda, 1998: Evolution of the morphology and microphysics of contrail cirrus from airborne remote sensing. *Geophys. Res. Lett.*, 25, 1153-1156.

Measurement of the Diffuse Radiation Fields Reflected by Clouds We've tackled, for the first time, the problem of achieving a **complete** bidirectional reflectance for a well-defined cloud deck. By **complete**, we mean 90° in zenith and 360° in azimuth, or the so-called bulk scattering phase function. This parameter is important for cloud remote sensing and retrievals (e.g., cloud albedo, optical thickness, particle size, etc.). Yet it has been difficult to acquire. We addressed this problem by measuring the diffuse radiation fields reflected by clouds during Arctic Radiation Measurement in Column Atmosphere-surface System (ARMCAS), June 1995, and First ISCCP Regional Experiment-Arctic Cloud Experiment (FIRE-ACE), June 1998. We acquired these measurements from University of Washington aircraft using a Goddard scanning radiometer (Figure 6). Figure 7 illustrates the bidirectional reflectance of an arctic stratus cloud deck, acquired during FIRE-ACE, as a function of zenith and azimuth angle at the red channel (0.68 μm). We obtained these measurements with the solar zenith angle at 53.65° . Of particular interest in these measurements is the enhanced backscattering maximum that occurs in opposition to the sun (antisolar direction where $\theta = 53.65^\circ$ and $\phi = 180^\circ$). Surrounding this glory feature is a pronounced rainbow, characteristic of water droplet clouds present in the Arctic at this time of year (29 May 1998). The glory, or the so-called Brocken bow or Bishop's ring, is often observed as rings around a plane's shadow when an airplane flies in the sunshine above clouds. The size of the glory depends on the size of cloud droplets (or crystals). In contrast, a complete rainbow cannot be perceived by common airplane or satellite observations, due to distance or restricted field of view. The primary rainbow is the light ray that enters the eye (or instrument) making a 42° angular circle (for red light) about the antisolar direction. This is predicted by the Snell's law that light strikes each spherical droplet and undergoes two refractions and one internal reflection before reaching the observer. The horizontal rainbow shown in Figure 7 is actually the intersection of the rainbow cone with the cloud deck. If the sun elevation ($90^\circ - \theta$) is greater than 42° , the rainbow will be an ellipse (otherwise, a hyperbola) and will turn into a circle for overhead

sun. These detailed measurements of optical phenomena will help us to better understand the retrieved cloud properties.

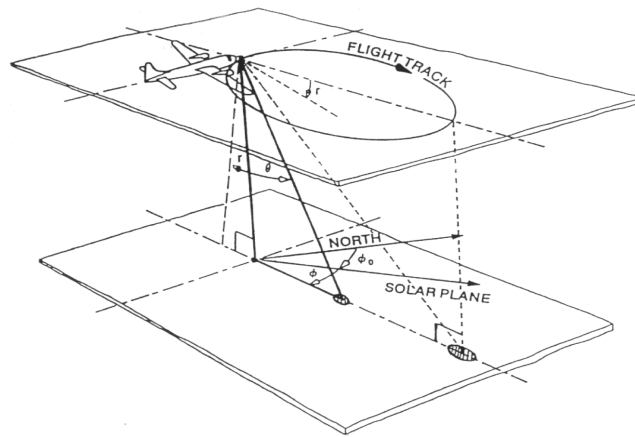


Figure 6. Schematic illustration of a clockwise circular flight track for measuring both the reflected and transmitted solar radiation. The radiometer, which scans from zenith to nadir on the starboard side of the aircraft with a scan rate of 100 rpm, maps out the entire reflection pattern of the surface during a complete circular orbit of the aircraft, which takes approximately 2.5 min. Every scan of the radiometer maps out a region on the Earth's surface displaced only 1.5° in azimuth. With a 1° field of view of the radiometer, a complete bi-directional reflectance of a surface can be obtained for 8 wavelengths of the radiometer simultaneously, as described in more detail by King (1992) and Tsay et al. (1998).

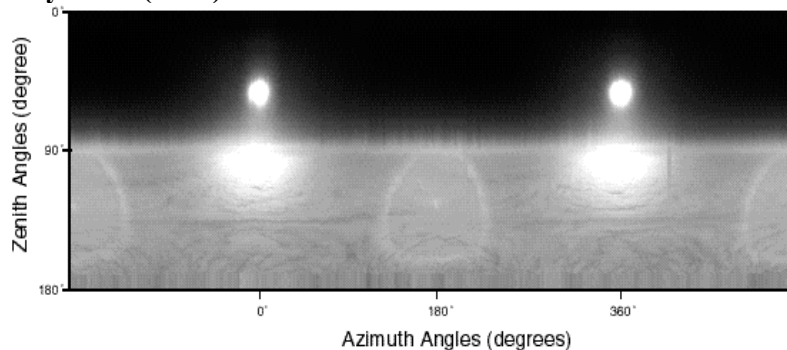


Figure 7. A complete cycle of measurements for both the sky radiance (upper half of the image strip 0°-90°, 0° for zenith) and reflected radiance (lower half 90°-180°, 180° for nadir) in a series of circular flight tracks during FIRE-ACE. Notice the solar disk (bright spots in the upper part) and the corresponding enhanced forward scattering from the clouds toward solar directions (at or around 0°/360° azimuth), the glory (bright spots in the lower part), and the rainbow (bright bands in the lower part) toward antisolar directions (at or around 180° azimuth).

Tsay, S.-C., M. D. King, G. T. Arnold, and J. Y. Li, 1998: Airborne spectral measurements of surface anisotropy during SCAR-B. *J. Geophys. Res.*, **103**, 31,943-31,953.

Remote Sensing of Tropical Cyclones Our analysis of satellite data and our participation in the third Convection and Moisture Experiment have taught us much about tropical storms. We've recently gained insight into the rapid intensity change of Hurricane Opal (1995) and Supertyphoon Paka (1997) from frequent passive microwave sensor observations on board the Defense Meteorological Satellite Program (DMSP), SSM/I, and TRMM Microwave Imager (TMI). These observations reveal rapid variations in the tropical cyclone eyewall latent heating. We hypothesize that these variations occur in the form of unusually long-lived, deep, and intense bursts of convective precipitation near the eye. The TMI and TRMM Precipitation Radar (PR) divulge significant fine-scale precipitation structures embedded within these bursts. For instance, these observations show an early, closed eye where none is apparent in conventional infrared imagery. The presence of an already closed eye suggests that the storm was deepening rapidly, whereas intensity estimates derived from traditional cloud-pattern-based techniques suggested a more immature storm with little likelihood of deepening. We investigated the connection between deep convection and electrification in the early stages of tropical cyclogenesis for a well-documented case of storm formation in the Coral Sea during the TOGA-COARE. This storm, Tropical Cyclone Oliver (1993), was intensively probed from the vantage point of several NASA aircraft sensors, including lidar, passive

microwave, active radar, and electric field/lightning detection. We found vigorous convection penetrating to nearly 18 km in the forming outer rainband. The convection generated substantial lightning and also contained the unusual event of supercooled liquid water at temperatures below -40 C. The eyewall convection, while shallower and devoid of lightning, nevertheless produced strong electric charging. We simulated these two distinct populations of deep cloud using a time-dependent one-dimensional model with sophisticated microphysics and an electrical parameterization scheme. We found differences in lightning flash production to be due primarily to updraft strength and relative concentrations of various rimed ice species present during cloud growth. Further studies involving remote lightning sensors (such as that currently flying on TRMM) could introduce electrification as one or more branches in the forecast decision tree involving the formation and intensification of tropical cyclones. The Laboratory also participated in the third Convection and Moisture Experiment (CAMEX-3) conducted during August and September. Based at Patrick Air Force Base, FL, the NASA-instrumented DC-8 and ER-2 flew coordinated hurricane research missions with the University of North Dakota cloud microphysics aircraft and two additional aircraft of the NOAA's Hurricane Research Division. Four tropical storms, including Hurricanes Bonnie and Georges, were investigated during different stages including genesis, maturity, and landfall. An unprecedented, high-quality data set was obtained, including hundreds of dropsondes made into and around these storms, *in situ* microphysical and electrification measurements, ER-2 Doppler Radar (EDOP) structure of deep eyewall and rainband convection, and numerous TRMM overflights.

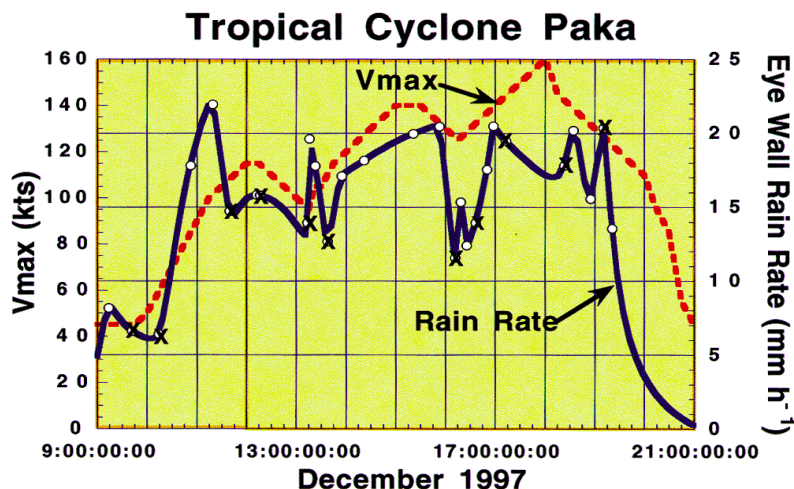
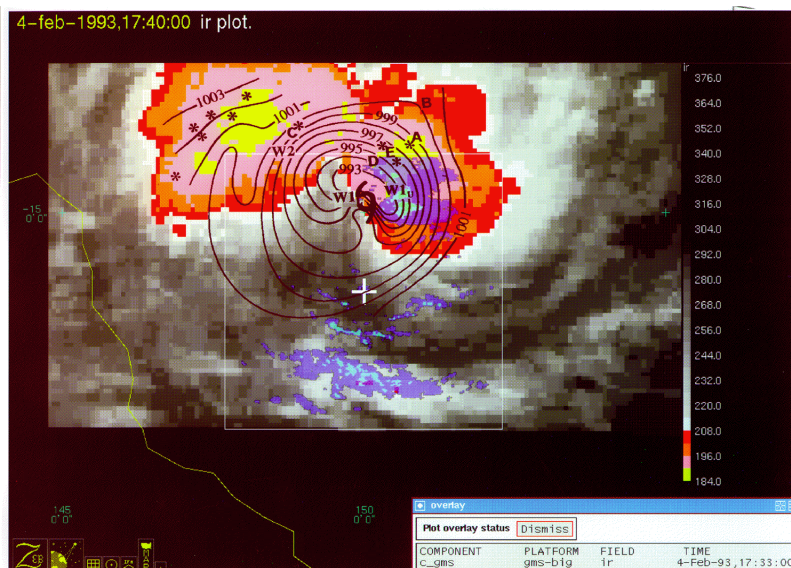
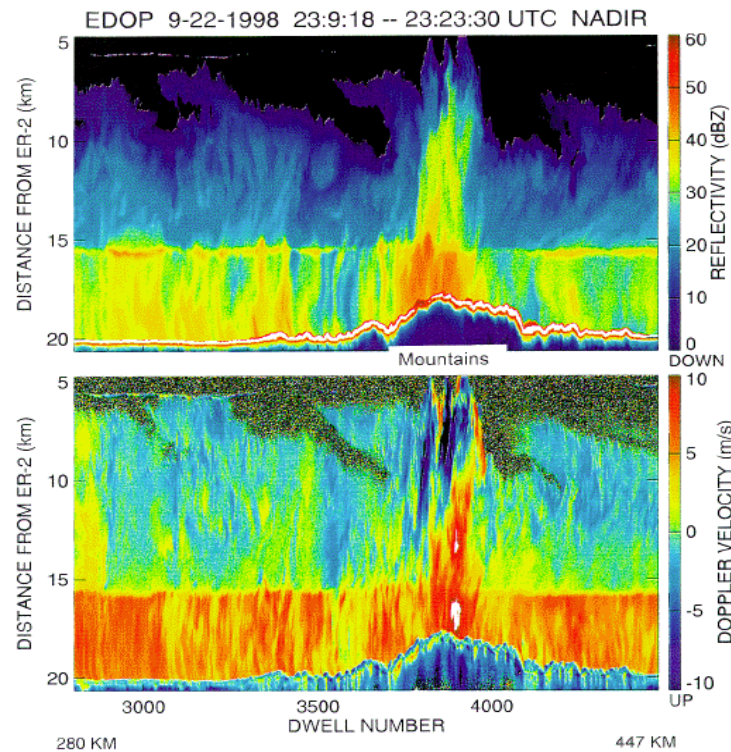


Figure 8. Paka's maximum winds (kts, dashed line) and SSM/I (O) and TMI (X) derived mean eyewall rain rate (mm h⁻¹, solid line) for the period between 0000 UTC on 9 December to 0000 UTC on 21 December. Maximum winds are obtained using the Dvorak technique. The eyewall rain rate is a spline fit made to the satellite observations. Three peaks in eyewall rainfall (used here as a proxy for latent heat release) correlate well with the three rapid intensification periods --- particularly from 10-11 December, when an eyewall convective burst was active. Note also the rapid and abrupt changes in eyewall-inferred latent heating.



Tropical Cyclone Oliver

Figure 9. Color overlay of Willis Island radar echo patterns (blue shades) on a Geostationary Meteorological Satellite (GMS) color-enhanced infrared satellite image of T.C. Oliver. Red cloud areas represent cloud tops colder than 208 K (14 km), while the yellow is 184 K (16.5 km). Two mesoscale convective systems (MCSs) with embedded vortices are shown interacting during the genesis stage of this storm. Black hurricane symbol denotes the pressure and wind vortex center and solid lines are isobars. Locations of the deepest convection are shown at A-E. Asterisks denote ten locations of strong electric fields, with all observed lightning contained in the western MCS.



Hurricane Georges --

Figure 10. Height-time cross section through deep convection in Hurricane Georges as revealed by EDOP during the storm's interaction with elevated terrain over the Dominican Republic. Both the reflectivity (top panel) and Doppler-derived vertical velocity (bottom panel) are shown. Note the location of deepest convection (15 km) over the mountains in the right side of the figure.

Rodgers, E. B., W.S. Olson, V. M. Karyampudi, and H. F. Pierce, 1998: Satellite- derived latent heating distribution and environmental influences in Hurricane Opal (1995). *Mon. Wea. Rev.* , **126**, 1229-1247.

Simpson, J., J. B. Halverson, B. S. Ferrier, W. A. Petersen, R. H. Simpson, R. Blakeslee, and S. L. Durden, 1998: On the role of "Hot Towers" in tropical cyclone formation. *Met & Atmos. Physics* , in press.

Rainfall Studies

Improving Global Data Sets Using TRMM and SSM/I-Derived Rainfall and Moisture Observations

The DAO is the first among the producers of global analyses to demonstrate the benefits of assimilating TRMM precipitation data into a global data assimilation system. We have developed a procedure to assimilate TRMM and SSM/I-derived rain rate and total precipitable water (TPW) estimate into the GEOS DAS. We found that using these data is very effective in improving the hydrological cycle and atmospheric energetics in the global analysis, as shown in Figures 11 and 12. Assimilating TRMM rain rates improves not only tropical precipitation in the analysis but also precipitation-related assimilation fields such as the outgoing longwave radiation, clouds, surface radiation, and the large-scale circulation. Using TRMM data in conjunction with the SSM/I-derived rainfall and TPW, bolsters these improvements. Specifically, rainfall assimilation reduces the state-dependent systematic errors in clouds and the cloudy-sky radiation, while TPW assimilation reduces errors in the moisture field to improve the longwave radiation in clear-sky regions. The improved analysis also

enhances the short-range forecast, but the improvement is modest compared with those in the time-averaged climate signals. This work shows that assimilation of satellite rainfall and TPW data can significantly improve the overall quality of 4-dimensional global climate data sets.

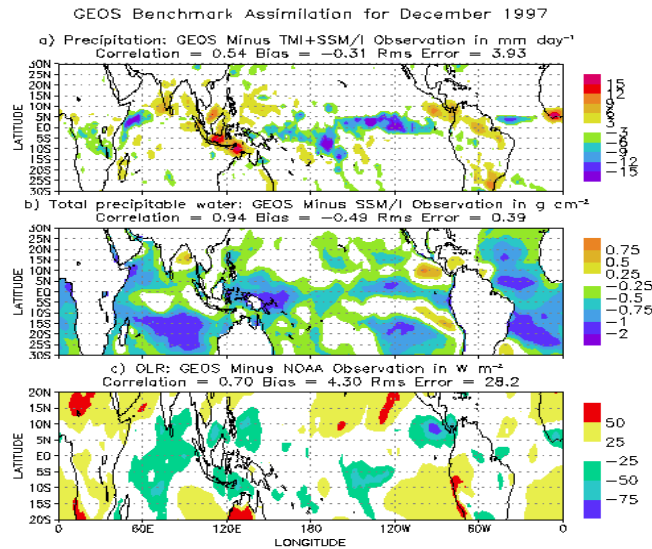


Figure 11. Differences in (a) precipitation, (b) total precipitable water, and (c) outgoing longwave radiation between satellite observations and the benchmark GEOS assimilation.

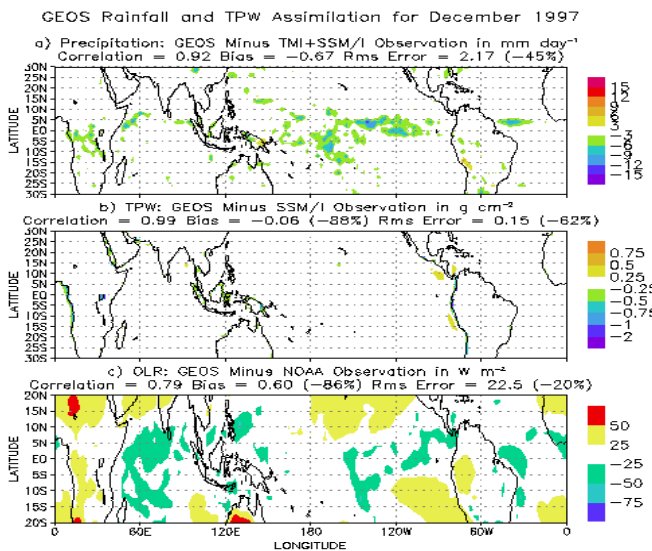


Figure 12. Differences in (a) precipitation, (b) total precipitable water, and (c) outgoing longwave radiation between satellite observations and the benchmark GEOS assimilation.

between satellite observations and the GEOS assimilation incorporating TRMM and SSM/I rainfall and TPW estimates. The percentage error reductions in these fields are given in parentheses.

Hou, A. Y., D. V. Ledvina, A. M. da Silva, S. Q. Zhang, J. Joiner, R. M. Atlas, G. J. Huffman, and C. D. Kummerow, 1999: Assimilation of SSM/I-derived surface rainfall and total precipitable water for improving the GEOS analysis for climate studies. *Mon. Wea. Rev.*, submitted.

Early Results from the TRMM Research centered around new TRMM data is proceeding along many different paths in the Mesoscale Atmospheric Processes Branch. Some of the highlights are given below. Research is being conducted to improve the Convective Stratiform separation in the Goddard Profiling Algorithm (see Hong et al., 1998). When the algorithm was applied to TRMM data, the higher spatial resolution immediately revealed that the procedure could be further improved by identifying stratiform rainfall that was either far from or unassociated with convection. This led to a significant improvement not only in the TMI rainfall but also in SSM/I version of the algorithm itself. During the hurricane season, TRMM data was used to gain new insight into strengthening of tropical cyclones. Simpson et al. (1998) concentrated on super typhoon Paka, which was captured soon after the TRMM launch. Strong convective bursts in the hurricane eyewall appear to be well correlated with future intensification. Similar findings to those described by Simpson et al. have been observed more recently in hurricane Bonnie as it moved toward the US mainland. A quantitative method for estimating latent heating rates from satellite microwave observations has been developed, tested, and applied to data from the SSM/I instrument with encouraging results (see Olson et al., 1998). Latent heating distributions derived from SSM/I observations of Hurricane Andrew show an increase in mid- and upper-tropospheric heating rates in the inner core of the storm as it undergoes a period of moderate intensification. Latent heating estimates are also compared to rawinsonde network estimates of total heating in the tropical Western Pacific. The algorithm is now being applied to the TRMM Microwave Imager, which promises even better results due to its higher spatial resolution. Over the last five years, methods have been developed to combine independent precipitation estimates into a best estimate in the region of data coverage. This approach is being applied operationally to produce global monthly fields from SSM/I, infrared, and rain gauge data under the Global Precipitation Climatology Project (see Huffman et al., 1997). The combination approach has been modified for TRMM to take the TMI/PR precipitation estimate as the standard of excellence and to exploit the near-coincident record of VIRS IR and TMI/PR data. First results from TRMM have demonstrated the key role that both modifications play in making accurate combinations.

Dec. 19, 1997 (336)

Dec. 19, 1997 (336)

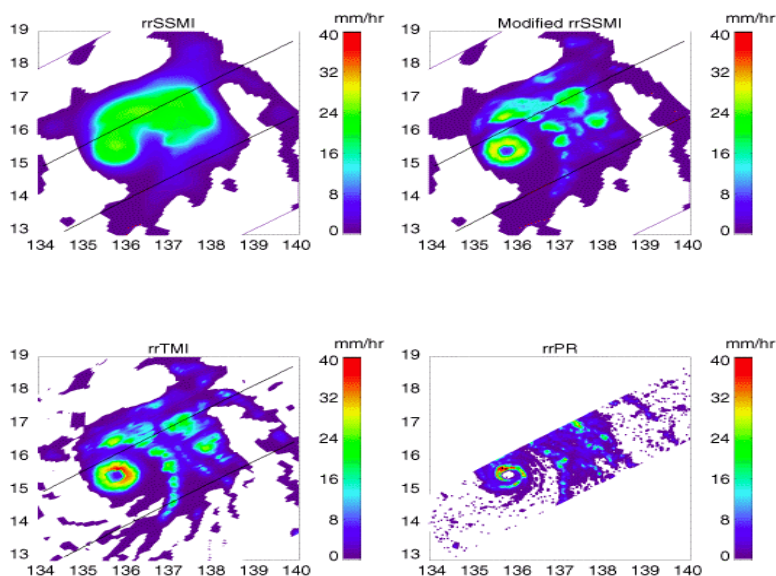


Figure 13. Comparison of rainfall rates derived from SSM/I with pre-TRMM algorithm (top left); SSM/I with the TRMM algorithm (top right); TMI (bottom left) and Precipitation Radar (PR) from TRMM (bottom right).

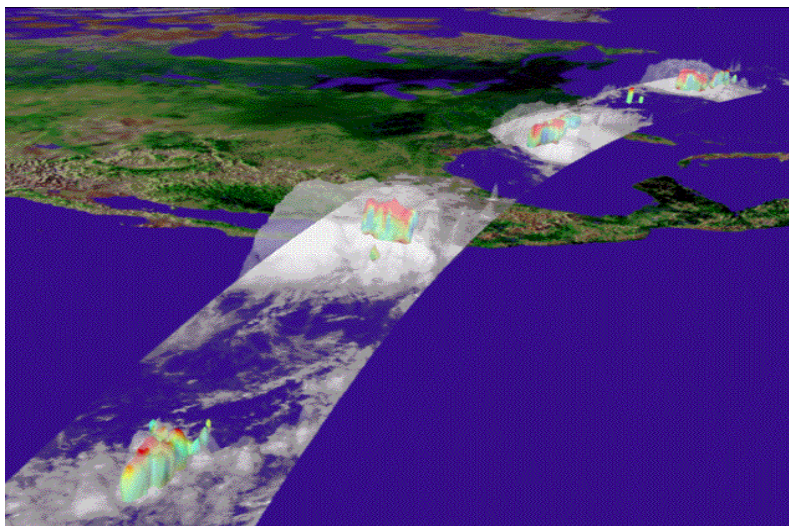


Figure 14. Tropical Storm Howard, Hurricane Isis, Hurricane Earl and Hurricane Danielle all line up under TRMM, passing over the scene from West to East on Sept. 2, 1998.

Hong, Y., C. Kummerow, and W. S. Olson, 1998: Separation of convective/stratiform precipitation using microwave brightness temperature. *J. Appl. Meteor.* , conditionally accepted.

Hong, Y., C. D. Kummerow, and W. S. Olson, 1998: Atmospheric latent heating distributions in the tropics derived from satellite passive microwave radiometer measurements. *J. Appl. Meteor.* , in press.

Simpson, J. , J. Halverson, H. Pierce, C. Morales, and T. Iguchi, 1998: Eyeing the eye: Exciting early stage science results from TRMM. *Bull. Amer. Meteor. Soc.* , **79**, 1171.

Huffman, G. J., R. F. Adler, P. Arkin, A. Chang, R. Ferraro, A. Gruber, J. Janowiak, A. McNab, B. Rudolf, and U. Schneider, 1998: The Global Precipitation Climatology Project (GPCP) combined precipitation dataset. *Bull. Amer. Meteor. Soc.* , **78**, 5-20.

Aerosol Studies

The Radiative Effects of Dust on Climate

In a paper published in *Nature*, we reported on a study of the response of the climate --- the air temperature --- to the radiative effects of dust aerosol. Models can calculate the impact of dust on the atmosphere and climate, but measuring the impact is very difficult. Moreover, the optical properties of dust aerosol are not well understood. In this study, we "tricked" nature to reveal its secrets. We examined the corrections, or errors, in model assimilation of the temperature field off the west coast of Africa, an area with heavy dust loading. The model includes most atmospheric processes but not aerosol. Therefore, the errors are affected by the presence of dust. By observing the correlation between the errors and satellite measurements of the dust presence, we were able to deduce the impact of the dust on the atmospheric temperature. The work represents a collaboration among Israeli, GSFC, and French scientists, all visiting or working at GSFC. It shows a new pathway for studying climate and human impact on climate using a combination of global

circulation models and satellite data.

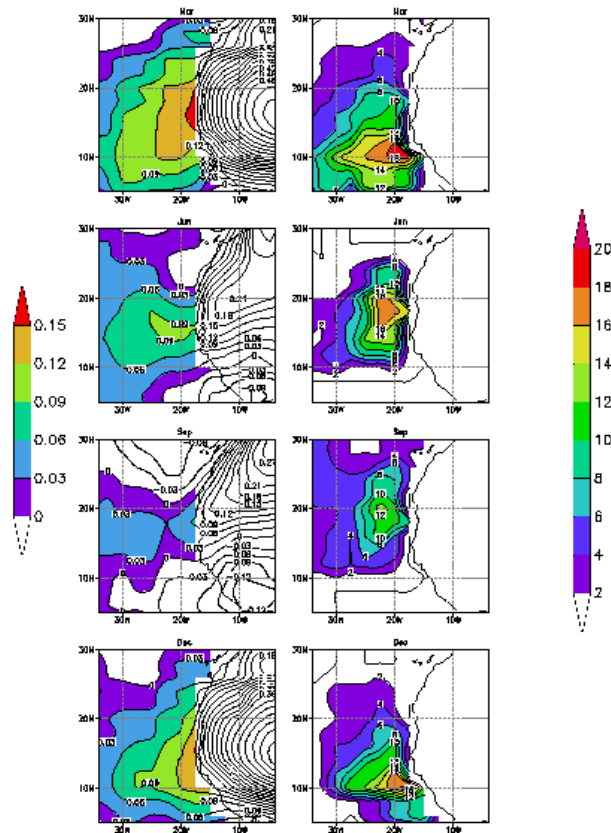


Figure 15. Right: Monthly average image of the number of dusty days for five years from 1984 to 1988 for March, June, September and December, top to bottom taken from a study by Jankoviak and Tanre (1992). Color represents the number of days by step of 2 as indicated on the bar to the right. Left: corresponding incremental analysis updates for temperatures, IAU(T), averaged during 1985-89, at the layer of 700-850 hPa. Shading corresponds to positive values over the ocean which correspond to a warmer atmosphere than predicted by first guess from the model. Contour interval is 0.03 K/d. Shading calibration is shown on the color bar to the left. The Televised Infrared Operational Satellite (TIROS) Operational Vertical Sounder (TOVS) was the primary observational source for the IAU over the ocean. The low-tropospheric TOVS temperature estimates have a slight negative bias over the study domain, which suggests that the IAU heating values may be underestimated. The maxima IAU(T) over the ocean of -0.1K/d are close to the maxima found over the tropical or subtropical oceans.

Alpert, P., Y. J. Kaufman, Y. Shay-El, D. Tanre, A. da Silva, S. Schubert, Y. H. Joseph, 1998: A first inference of atmospheric response to dust forcing from a Data Assimilation System. *Nature*.

Interannual Trends and Variability of East Coast Aerosol Every year, the summer months bring hazy conditions to the United States' eastern seaboard. Modeling efforts show that the high aerosol loadings that create the haze may contribute to the radiative forcing of climate. These modeling studies assume that the aerosol consists mainly of sulfate particles that are formed from industrially emitted SO₂ gas. However, recent observations suggest that much of the aerosol consists of organics that may be of natural, biogenic origin. If the aerosol particles are organics and not sulfates, how much of the optical thickness and subsequent radiative forcing is natural and how much is human-induced? The U.S. Environmental Protection Agency (EPA) has noted a significant downward trend in SO₂ concentrations at stations near

2

NASA Goddard Space Flight Center in Greenbelt, MD (Figure 16). If the industrial component of the aerosol contributes significantly to the aerosol light scattering, the optical thickness should also show a downward trend. Figure 16 shows that, indeed, summertime mean optical thickness appears to decrease from the early 80s to the present, similar to the downward trend in SO_2 . However, meteorological factors have not yet been eliminated so cause and effect have not yet been established. The aerosol optical thickness varies from year to year and exhibits a downward trend. Still, the aerosol size distribution appears to remain unchanged. We see this from the spectral dependence of the optical thickness (not shown) and from the phase function (Figure 17) analyzed from in-depth analysis of two years of data. The interannual variation of the phase function is less than 7% for situations of heavy aerosol loading. The consistency in aerosol is a welcome result for both long-term climate modeling and remote sensing applications.

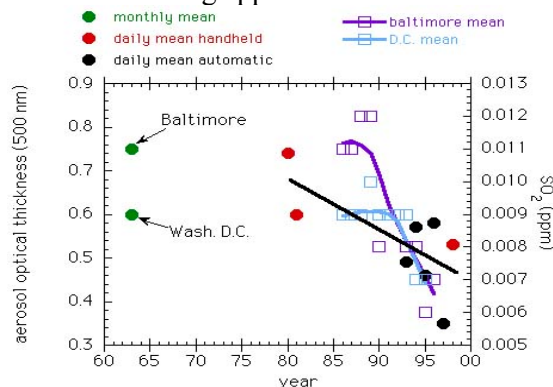


Figure 16. Time series of mean summer (June-August) aerosol optical thickness at 500 nm measured at the NASA GSFC in Greenbelt MD or nearby sites. The green points are taken from Flowers et al. (1969) and were calculated from multi-year monthly values of the early 60s. The two values representing the summers of '80 and '81 were taken from Kaufman and Fraser (1983). The red and black points were calculated from daily mean values with the red points consisting of hand-held measurements and the black points consisting of automatic AERONET measurements. The black line is the linear trend of the points from 1980-1998. The squares and blue and purple curves represent annual mean values and trends, respectively, of SO_2 concentrations measured by the EPA at sites in Washington D.C. and Baltimore. The SO_2 values can be read from the graph on the right hand axis.

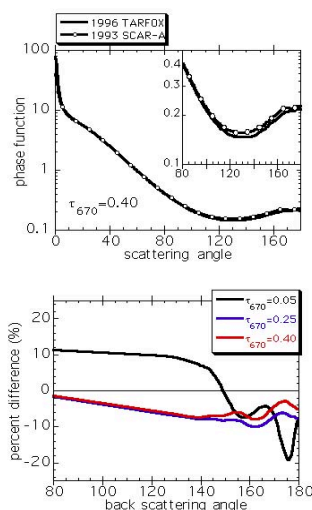


Figure 17. (top) The phase function calculated from the aerosol models derived from 1993 and 1996 data (Remer and Kaufman, 1998) for optical thickness of 0.40 at 670 nm. The insert shows the backscattering portion enlarged. **(bottom)** The difference in phase function between the two years, 1993 and 1996, for three optical thicknesses showing the backscattering portion only. (Remer et al., 1998).

Flowers, E.C., R. A. McCormick and K. R. Kurfis, 1969: Atmospheric turbidity over the United States, 1961-1966. *J. Appl. Meteor.*, **8**, 955-962.

Kaufman, Y. J. and R. S. Fraser, 1983: Light extinction by aerosols during summer air pollution. *J. Clim. & Appl. Meteor.* , **22**, 1694-1706.

Remer, L. A. and Y J. Kaufman, 1998: Dynamical aerosol model: Urban/industrial aerosol. *J. Geophys. Res.* , **103**, 13,859-13,871.

Remer, L. A., Y J. Kaufman and B. N. Holben, 1999: Interannual variation of ambient aerosol characteristics on the east coast of the United States. *J. Geophys. Res.* , **104**, 2223-2231.

U.S. Environmental Protection Agency, National Air Quality and Emissions Trends Report, 1995. EPA document 454/R-97-013, 1997.

Data Assimilation Studies

Enhanced Impact of NASA Scatterometer Data on Weather Analysis and Forecasting

Our initial evaluation of NASA Scatterometer (NSCAT) data demonstrated the high quality of these data as well as their potential to improve ocean surface analysis and weather prediction. Experiments with the GEOS-1 DAS showed very significant improvements in surface wind and sea level pressure analyses over the Southern Hemisphere oceans. In addition, useful weather forecast skill for the Southern Hemisphere extratropics was extended by approximately 24 hours. In the Northern Hemisphere, analysis improvements were much rarer and we could discern no improvement in the accuracy of numerical weather. Following these initial results, we conducted research to improve the impact of the NSCAT data in the Northern Hemisphere. To this end, we incorporated methodology into the evolving GEOS-2 DAS to treat the asynoptic (nonsynchronous) nature of the data. The results obtained from data-impact experiments with the GEOS-2 DAS are particularly noteworthy in that the control forecasts (without NSCAT data) are very much improved over those with GEOS-1, yet the impact of NSCAT data is increased. While the impact of NSCAT is still much larger in the Southern Hemisphere, a discernable improvement in the more data dense Northern Hemisphere forecast accuracy was obtained for the first time. This improvement demonstrates both the value of scatterometer winds and the importance of treating satellite data asynoptically. A refereed article on these results entitled "Geophysical validation of NSCAT winds using atmospheric data and analyses" by Atlas et al. has been accepted for publication in the Journal of Geophysical Research and will appear in January 1999.

Atlas, R., S. C. Bloom, R. N. Hoffman, E. Brin, J. Ardizzone, J. Terry, D. Bungato, and J. C. Jusem, 1998: Geophysical validation of NSCAT winds using atmospheric data and analyses. *J. Geophys. Res.*, submitted.

Atmospheric Variability and Predictability

The Development of the South Asian Summer Monsoon and the Intraseasonal Oscillation

The Asian summer monsoon undergoes pronounced interannual and intraseasonal climate fluctuation on both local and global scales. To understand monsoon variability, we need to know more about the nature of the coupling between the seasonal cycle and the 30-60 day global-scale low frequency intraseasonal oscillation (ISO). The ISO is predominantly an eastward propagating wave with zonal wave number 1. In this study we used fourteen years (1980-93) of data assimilated at NASA Goddard Space Flight Center to carry out an analysis of the variability in the development of the South Asian summer monsoon associated with the ISO. We found that the influence of the ISO on the development of the monsoon is both local and remote, and depends on the strength and phasing of the ISO with the monsoon seasonal cycle. Of the 14 years examined here, six showed a strong contribution by the ISO to the northeastward progression and onset of the monsoon rains over India. In these cases, the ISO is initially (about two weeks prior to the normal onset of rains over India) out of phase with the regions of large-scale rising and sinking motion, acting to suppress the seasonal development of the monsoon. As the ISO moves to the northeast, the rising branch enters the Indian Ocean, leading to enhanced heating

and precipitation in this region. At low levels, the ISO is linked to distinct circulation anomalies over the Arabian Sea and Indian Ocean, which act to initially inhibit and then accelerate the Somali jet. This low-level jet is instrumental in bringing water vapor to the Indian continent to fuel the monsoon rains. The coupling between the low-level and upper-level circulation is such that, as the ISO moves in phase with and enhances the seasonal mean upward motion, there is an abrupt and intense development of the low level southwesterly winds (the Somali Jet) leading to an unusually rapid northeast shift and intensification of the monsoon rains over India and the Bay of Bengal. In this way, the influence of the ISO on the monsoon may be viewed as an initial suppression and then acceleration of the 'normal' seasonal cycle of the monsoon.

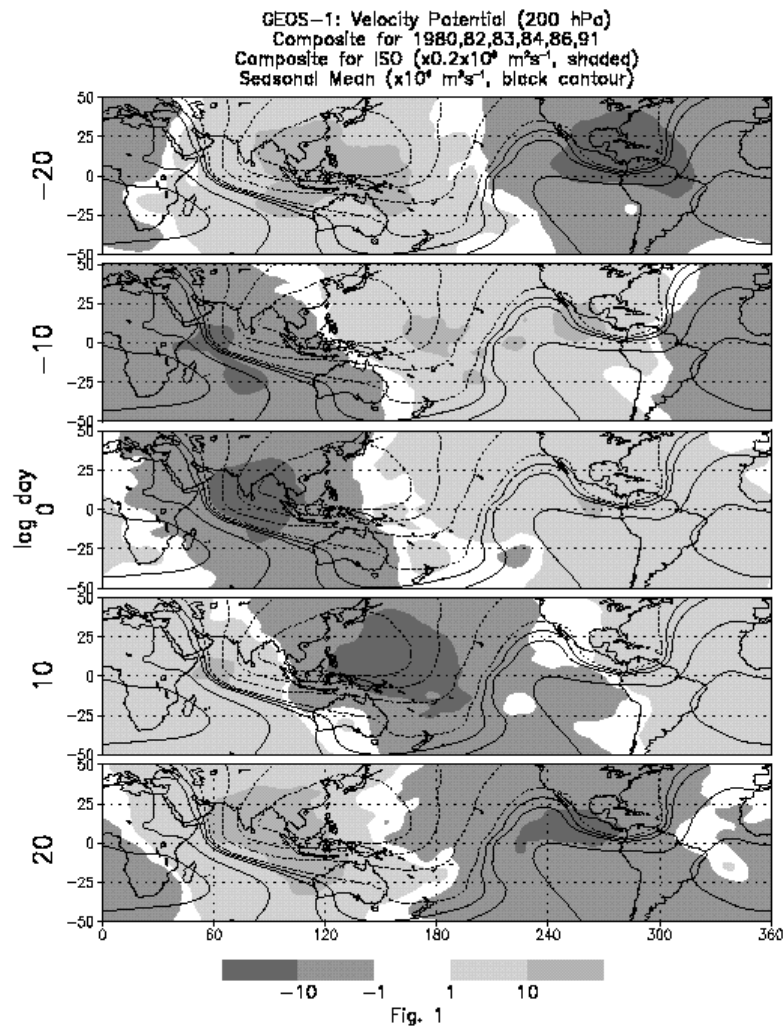


Figure 18. Composite average velocity potential for the ISO onset years (1980, 82, 83, 84, 86, and 91). Lag 0 is the time of maximum rainfall over India based on the ISO index. Members of the composite have a 20-70 day filter

applied. The contours repeated in each panel are for the June-August mean (1980-93) velocity potential.

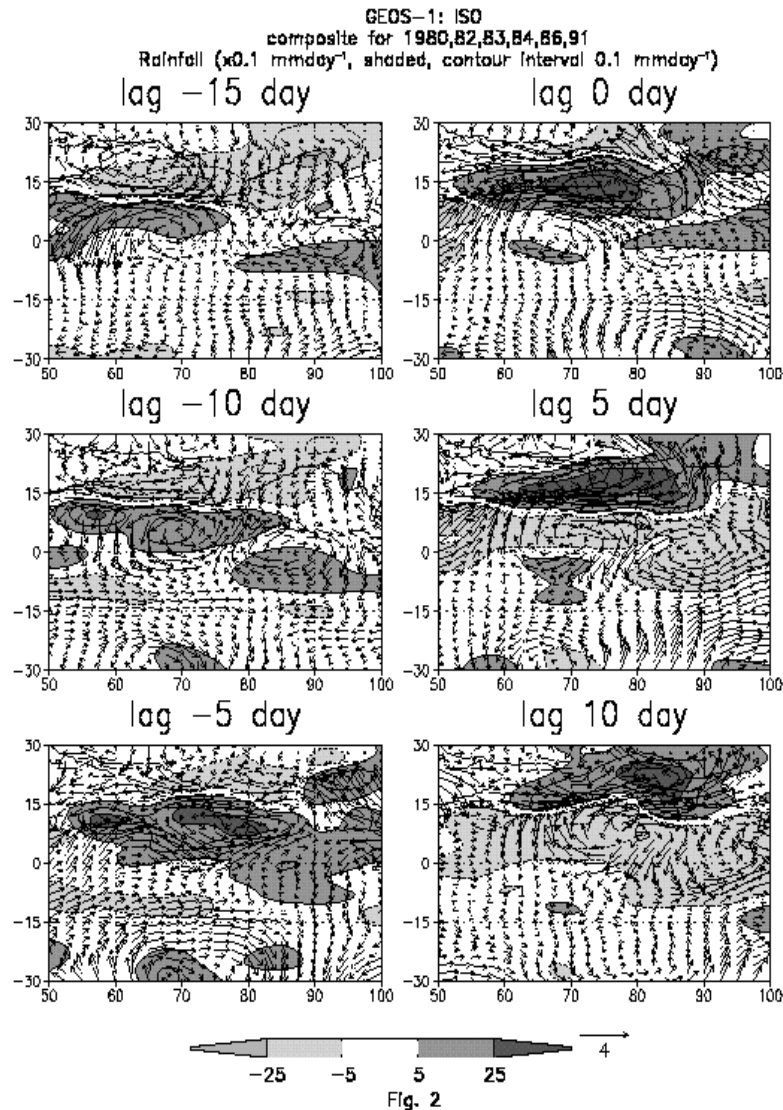


Figure 19. The same as Figure 18, except for the 85 hPa winds and precipitation.

Wu, M.-L., S. Schubert, and H. E. Huang, 1999: The development of the south Asian monsoon and the intraseasonal oscillation. *J. Clim.*, to appear.

Global Warming Estimation from MSU We've devised a means of analyzing microwave radiometer data to improve the accuracy with which we can monitor global temperature from space. Microwave radiometer observations from space allow us to monitor global temperature and its long term variation. This capability is due largely to the ability of the microwave radiometers to see through clouds in the atmosphere. Spencer and Christy (1990) pointed out for the first time that the observations made by the Microwave Sounding Unit (MSU) radiometer in Ch 2 (53.74 GHz) correlated well with other measurements of global temperature. Thus, the MSU data taken from the NOAA operational satellite series from 1979 constitutes the basis for these studies. However, because different MSU instruments were flown on successive satellites, we experience problems while developing a continuous time series of Ch 2 data. The problems are largely systematic in nature and can be removed by careful analysis. The recent analysis of global temperature from MSU data by Christy et al. (1998) did not properly adjust for these systematic errors. As a result, that analysis showed a global cooling from 1979-1997. In particular, one systematic error related to the NOAA 11 orbital drift introduced an error of about 0.17 K in their analysis. In our research, we carefully examined this systematic error and found it to yield misleading results. When we adjust for the effort, the resulting time series yields a global warming of about 0.12 K per decade with an

uncertainty of 0.06 K per decade. This result is strongly substantiated in our study with the help of detailed statistical analysis of the MSU data. The global warming deduced in our study is consistent with that of the conventional data analysis of the surface temperature.

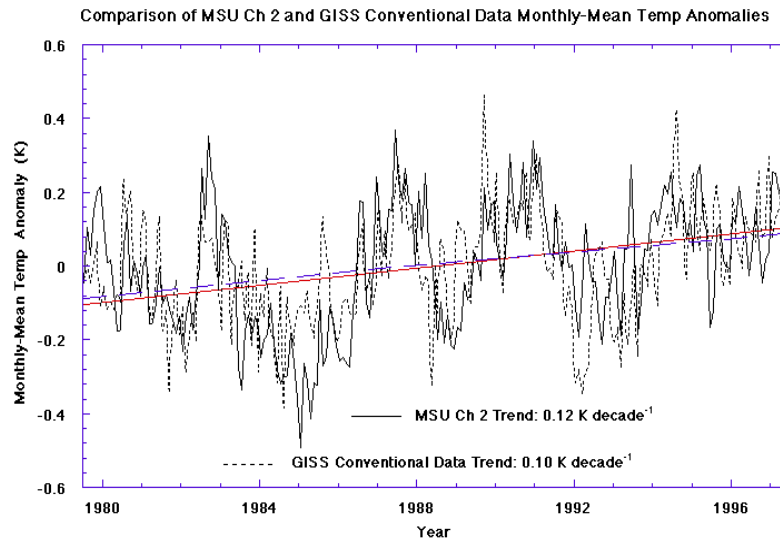


Figure 20. Comparison of MSU Ch 2 and GISS conventional data monthly-mean temperature anomalies.

Prabhakara, C., R. Iacovazzi, Jr., J.-M. Yoo, and G. Dalu, 1998: Global warming deduced from MSU. *Geophys. Res. Lett.*, **25**, 1927-1930.

Modeling Studies The Use of the Goddard Cumulus Ensemble Model in Studies of Deep Tropical Convection for the GEWEX Cloud System Study and TRMM The primary goal of the GEWEX Cloud System Study (GCSS) Working Group 4 (WG4) is to understand and improve deep tropical cloud processes in GCM. GCM cannot resolve the individual convective cells in a grid box. Accordingly, we use cloud resolving models (CRMs) to resolve and quantify the collective effects of clouds that represent a single GCM column. We can then use the CRMs to examine the way large-scale processes relate to the development, maintenance, and structure of tropical cloud systems. The Goddard Cumulus Ensemble Model (GCE) participated in the GCSS WG4 Case 2 study. This study involved an 8-day simulation of deep tropical convection over the TOGA-COARE IFA during December 1992. A total of eight CRMs were involved in this intercomparison study, as well as eight Single Column Models (SCMs). The GCE model produced mean temperature and moisture errors that were smaller than the other CRMs and SCMs. The GCE used a 3-class ice microphysics parameterization (cloud ice, snow, and graupel), a shortwave and longwave radiation parameterization, and surface fluxes for air-sea transfer. Errors were larger for CRMs that included only a 2-class ice scheme (cloud ice and snow). This difference indicates the importance of microphysical processes in the energy budgets of the convective system. The superiority of the CRMs over the SCMs is due largely to the greater spatial and temporal resolution in the CRMs and to the use of more sophisticated and physically realistic parameterizations of cloud microphysical processes and cloud-radiation interactions. The vertical distributions of convective latent heat release and moisture in the tropics lead to the modulations of large-scale tropical circulations, and, in turn, to the energy budgets on a global scale. The GCE was able to simulate the vertical heating (Q1) and moisture (Q2) profiles for the five convective events during December 19-27, 1992, with relatively small errors from the observed profiles. Rainfall can be estimated from the vertical distributions of convective latent heat release. Accordingly, GCE-simulated heating profiles such as these are being used within the Mesoscale Atmospheric Processes Branch in developing heating retrieval and rainfall algorithms for the TRMM. Accurate rainfall measurements in the tropics are important, since rainfall is a key link in the hydrologic cycle and the primary heat source for the atmosphere. GCE-derived atmospheric and cloud profiles at a single time during the active period of December 25, 1992, are being provided to other CRMs in an offline intercomparison of radiation and surface fluxes (see <http://rsd.gsfc.nasa.gov/users/djohnson/gcsswg4>). Initial results indicate that even with an identical atmospheric state, significant differences between the surface fluxes and radiation profiles exist between the CRMs (>20%). We will continue leading this project, with the goals of understanding and resolving these discrepancies between the CRMs, so they can be

more accurately used in developing cloud parameterizations in the GCM.

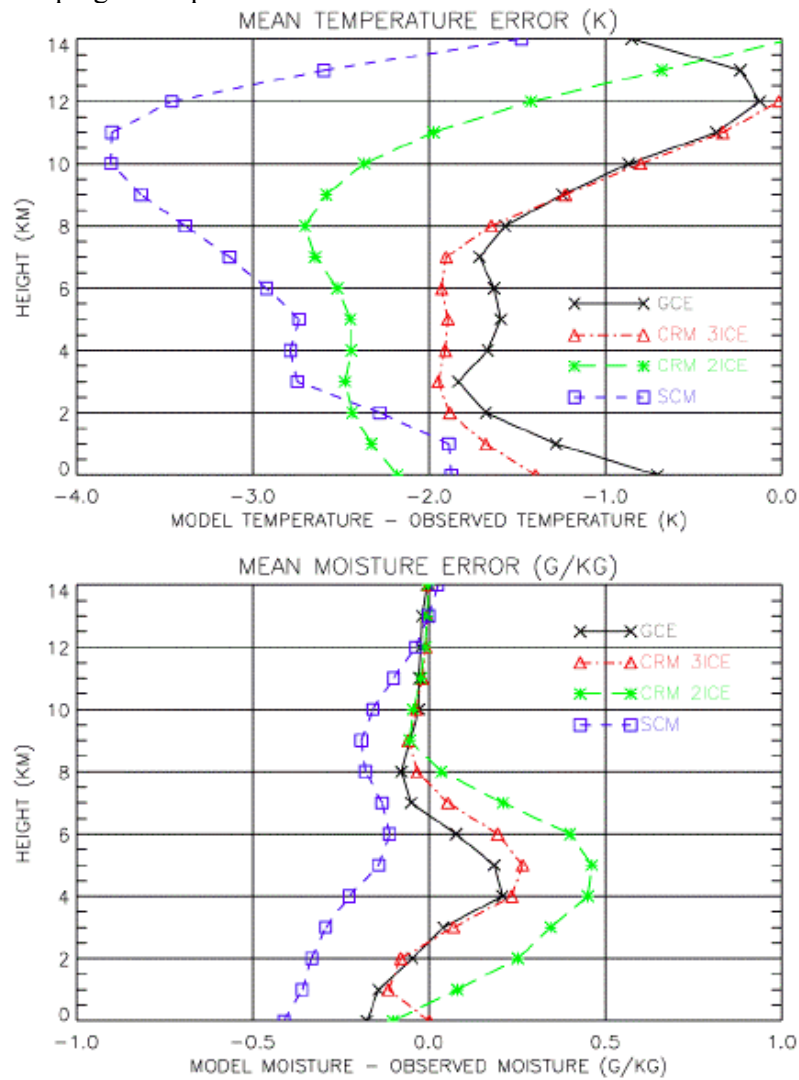


Figure 21. Mean temperature (K), and moisture (g/kg) errors for models participating in the GCSS WG4 Case 2. The solid line represents the GCE model, the dash-dot is CRMs with three ice species, the long dash is CRMs with

two ice species, and the short dash is SCMs.

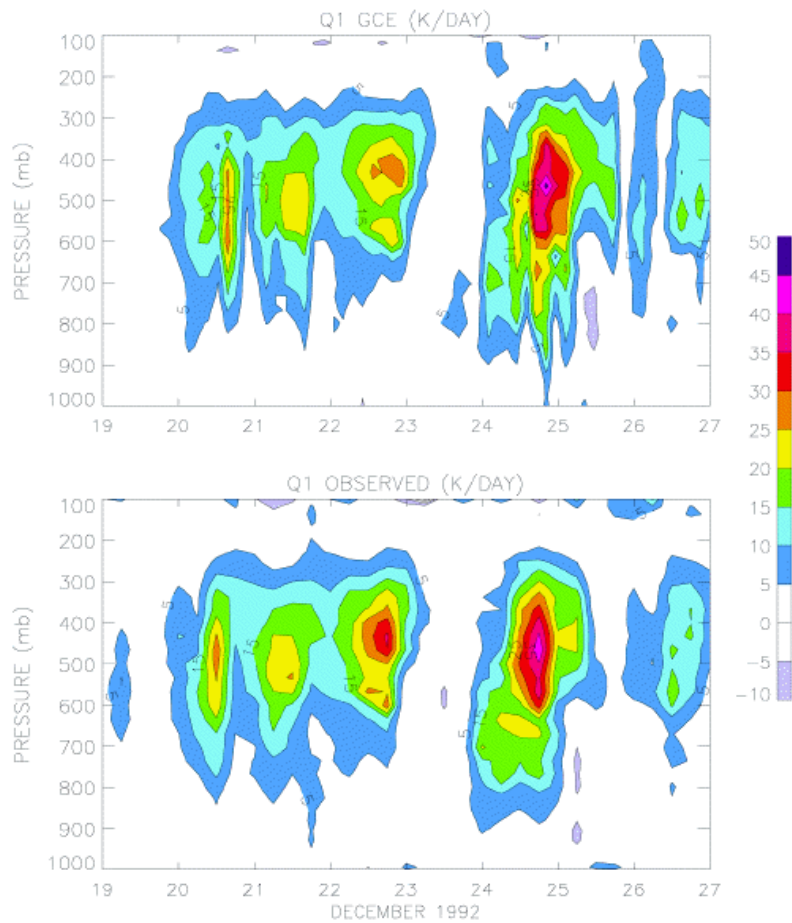


Figure 22. GCE domain-averaged and observed Q1 profiles over the TOGA-COARE IFA. Positive/Negative Q1

values represent warming/cooling (K/day) in the atmosphere.

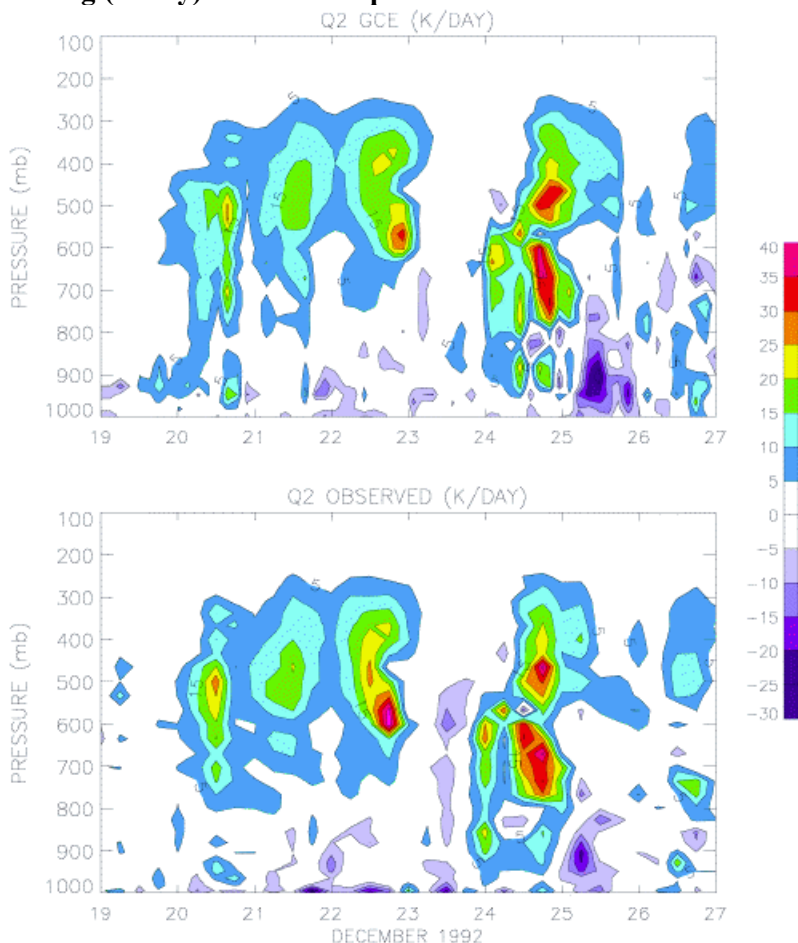


Figure 23. GCE domain-averaged and observed Q2 profiles over the TOGA-COARE IFA. Positive/Negative Q2 values represent the equivalent heating/cooling produced by the removal/addition of moisture (e.g. condensation/evaporation).

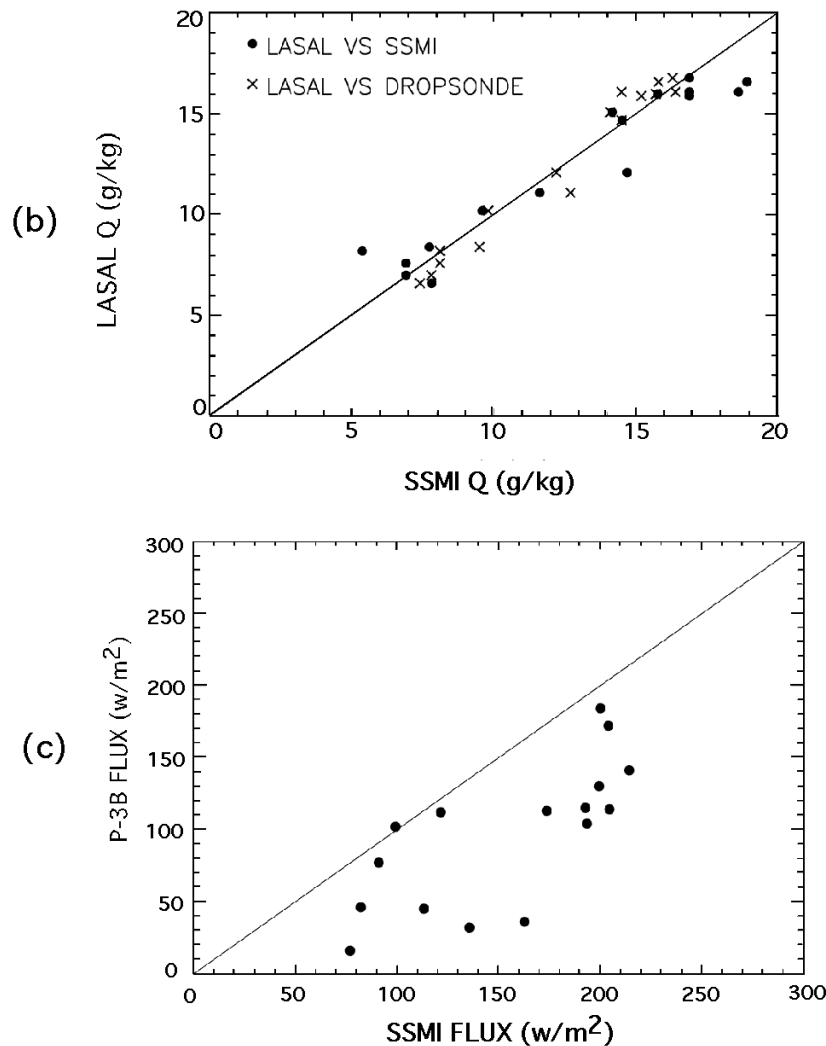
Johnson, D. E., W.-K. Tao, and J. Simpson, 1998: A study of the response of deep tropical clouds to mesoscale processes: Part I: Modeling strategies and comparisons with observations. to *J. Atmos. Sci.*, submitted.

Air-Sea Surface Fluxes

Air-Sea Latent Heat Flux Estimation from Lidar, Radiometer and Scatterometer Data

We've used data gathered during the Lidar In-space Technology Experiment (LITE) to derive latent heat flux over the tropical and sub-tropical ocean. For this mission, the NASA P-3B aircraft was equipped with the LASAL system, two microwave scatterometers, a multi-spectral radiometer, and dropsondes. We developed a technique to derive humidity structure in the boundary layer using the lidar and radiometer data. We then compared the results with *in situ* dropsonde measurements at 16 locations over the Atlantic Ocean. We found that near-surface specific humidity could be retrieved with an rms accuracy of 0.8 g/kg; and the average bulk boundary layer moisture content, to better than 0.7 g/kg. This technique uses lidar-derived statistics on the height of cumulus cloud tops to estimate the lifting condensation level (LCL) as shown in Figure 24. The figure shows lidar backscatter from a typical marine boundary layer, with the height of the layer superimposed on the image. The clouds are identified by the absence of a ground return, and a height distribution of the cloud tops is formed. The LCL is estimated from this distribution as that level below 95 percent and above 5 percent of the cloud tops. Combining the height of the LCL with an estimate of the near-surface air temperature (based on the radiometric sea surface temperature) yields the near-surface moisture (Palm et al., 1998). During the last year, we've analyzed the scatterometer-derived surface winds. We've used the surface winds with the near-surface moisture (Figure 25) to compute latent heat flux using the bulk aerodynamic flux scheme designed for use in the TOGA-COARE experiment. Since *in situ* measurements of heat flux are not available, we've used SSM/I latent heat flux derived from the method of Chou et al. (1997) for comparison. The results show that the SSM/I flux values are generally 40 to 50 percent larger than

the lidar-scatterometer estimate (Figure 24). Little if any of this difference is due to near-surface moisture, as SSM/I compares very favorably with the LASAL-radiometer retrieval (Figure 24). Rather, much of this bias is caused by (1) the SSM/I wind speed, which is greater than the airborne scatterometer measurement in 11 of the 16 cases, and (2) a difference in the bulk flux algorithm being used in the two studies. Further validation activities are required to understand the difference in flux magnitude. We conclude that a combination of scatterometer winds and lidar-radiometer-derived near-surface moisture provides a unique way to estimate the surface exchange of latent heat between the ocean and atmosphere. This work establishes a new technique for retrieving this important quantity. The technique should be applicable to spaceborne lidar systems of the near future, such as GLAS, scheduled for launch in mid 2001. Future analysis will relate the latent heat flux to other lidar-derived parameters such as boundary layer height, entrainment zone depth, and integrated lidar backscatter intensity.



(a) Comparison of lidar-radiometer retrieved near surface moisture with SSM/I and dropsonde values and (b) lidar-radiometer-scatterometer derived latent heat flux compared with the SSM/I estimate for 16 locations in the tropical and sub-tropical Atlantic Ocean.

Figure 24. (a) Comparison of lidar-radiometer retrieved near surface moisture with SSM/I and dropsonde values and (b) lidar-radiometer-scatterometer derived latent heat flux compared with the SSM/I estimate for 16 locations

in the tropical and sub-tropical Atlantic Ocean.

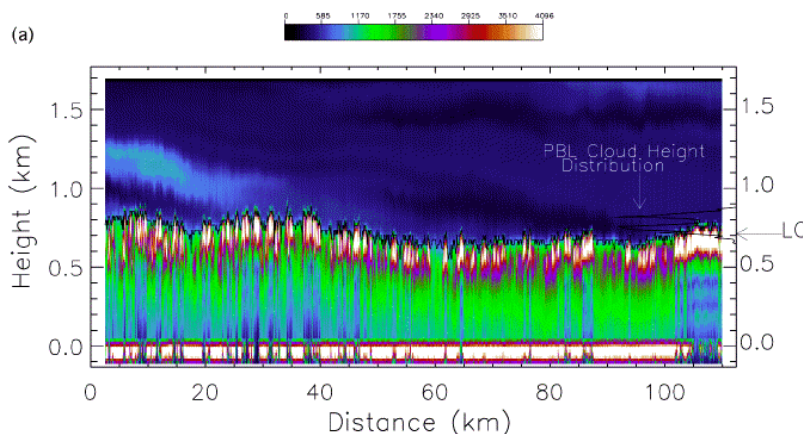


Figure 25. Lidar backscatter from a typical marine boundary layer with the height of the layer superimposed on the image. The clouds are identified by the absence of a ground return. This effect forms a height distribution of the cloud tops.

Chou, S.-H., C.-L. Shie, R. Atlas and J. Ardizzone, 1997: Air-sea fluxes retrieved from special sensor microwave imager data. *J. Geophys. Res.*, **12**, 12,705-12,726.

Palm, S. P., D. Hagan, G. Schwemmer and S. H. Melfi, 1998: Inference of marine atmospheric boundary layer moisture and temperature structure using airborne Lidar and infrared radiometer data, *J. Appl. Meteor.*, **37**, 308-324.

Galileo Results

The Composition of the Jovian Atmosphere as Determined by the Galileo Probe Mass Spectrometer

The Atmospheric Experiment Branch contributed the mass spectrometer instrument for the Galileo Probe mission that entered the atmosphere of Jupiter on December 7, 1995. The resulting data have been corrected for known instrumental effects and yielded the following results. The Galileo Probe Mass Spectrometer determined the composition of the Jovian atmosphere for species with masses between 2 and 150 atomic mass units from 0.5 to 21.1 bar. Constituents identified include H_2 , He, Ne, Ar, Kr and Xe, CH_4 , NH_3 , H_2O , H_2S , C_2 , C_3 non-methane hydrocarbons, and possibly PH_3 and Cl . $^4He/H_2$ in the Jovian atmosphere was measured to be 0.157 ± 0.030 . $^{13}C/^{12}C$ was found to be 0.0108 ± 0.0005 and D/H and $^3He/^4He$ were measured. Ne was depleted, ≤ 0.13 times solar, Ar ≤ 1.7 times solar, Kr $\leq 5 \times$ solar, and Xe $\leq 5 \times$ solar. CH_4 has a constant mixing ratio of $(2.1 \pm 0.4) \times 10^{-3}$ (^{12}C 2.9 times solar) where the mixing ratio is relative to H_2 . Upper limits to the H_2O mixing ratio rose from 8×10^{-7} at pressures less than 3.8 bar to $(5.6 \pm 2.5) \times 10^{-5}$ (^{16}O 0.033 ± 0.015 solar) at 11.7 bar and, provisionally, about an order of magnitude larger at 18.7 bar. The mixing ratio of H_2S was less than 10^{-6} at pressures less than 3.8 bar, but rose from about 0.7×10^{-5} at 8.7 bar to about 7.7×10^{-5} (^{32}S 2.5 times solar) above 15 bar. Only very large upper limits to the NH_3 mixing ratio have been set at present. If PH_3 and Cl were present, their mixing ratios also increased with pressure. Species were detected at mass peaks appropriate for C_2 and C_3 hydrocarbons. It is not yet clear which of these were atmospheric constituents and which were instrumentally generated. These measurements imply (i) fractionation of 4He , (ii) a local, altitude-dependent depletion of condensables, probably because the probe entered the descending arm of a circulation cell, (iii) that icy planetesimals made significant contributions to the volatile inventory, and (iv) a moderate decrease in D/H but no detectable change in $(D + ^3He)/H$ in this part of the galaxy during the past 4.6 billion years.

Niemann, H. B., S. K. Atreya, G. R. Carignan, T. M. Donahue, J. A. Haberman, D. N. Harpold, R. E. Hartle, D. M. Hunten, W. T. Kasprzak, P. R. Mahaffy, T. C. Owen, and S. H. Way, 1998: The composition of the Jovian atmosphere as determined by the Galileo Probe Mass Spectrometer. *J. Geophys. Res.*, **103**, 22,831-22,845.

Galileo Probe Measurements of D/H and $^3\text{He}/^4\text{He}$ in Jupiter's Atmosphere How can we determine the values of D/H and $^3\text{He}/^4\text{He}$ in the primitive solar nebula 4.5 billion years ago at the time the solar system formed? The best method is to measure these quantities in the present atmosphere of Jupiter. This procedure is valid under the widely accepted assumption that all but a negligible portion of the isotopes of the light gases found in the Jovian atmosphere today came directly from the gaseous nebula, and that no important contributions came from sources of fractionated hydrogen or helium, such as icy planetesimals. In the sun, the nebular D was converted to ^3He early in solar history, so these ratios cannot be obtained directly from present day solar values. The D/H protosolar ratio established by the Jovian measurements will help us understand the contribution of high-D/H icy planetesimals to the atmospheres of Uranus and Neptune and to the Earth's oceans. These values can also provide constraints on models of galactic evolution, since the D/H ratio in the universe is predicted to have decreased monotonically since the Big Bang. The value of the D/H ratio locked in Jupiter's atmosphere 4.5 billion years ago provides one reference point in an extrapolation from the present, precisely known value of this ratio in the local interstellar medium to the primordial value. The Galileo Probe Mass Spectrometer measurements in the atmosphere of Jupiter give: $\text{D}/\text{H} = (2.6 \pm 0.7) \times 10^{-5}$, $^3\text{He}/^4\text{He} = (1.66 \pm 0.05) \times 10^{-4}$. These ratios supercede earlier results by Niemann et al. (1996). They are based on a reevaluation of the instrument response at high count rates and on a more detailed study of the contributions of different species to the mass peak at 3 amu. The D/H ratio is consistent with Voyager, with ground-based data, and with recent spectroscopic and solar wind (SW) values obtained from the Infrared Spectroscopic Observatory (ISO) and Ulysses. The $^3\text{He}/^4\text{He}$ ratio is higher than that found in meteoritic gases $(1.5 \pm 0.3) \times 10^{-4}$. The Galileo result for D/H, when compared with that for hydrogen in the local interstellar medium $(1.6 \pm 0.12) \times 10^{-5}$, implies a small decrease in D/H in this part of the universe during the past 4.55 billion years. Thus, it tends to support small values of primordial D/H - in the range of several times 10^{-5} rather than several times 10^{-4} . These results are also quite consistent with no change in $(\text{D} + ^3\text{He})/\text{H}$ during the past 4.55 billion years in this part of our galaxy. The results, together with the terrestrial D/H ratio and three recent determinations of the D/H ratio in comets, imply that comets could have contributed a portion but not the entirety of the Earth's oceans.

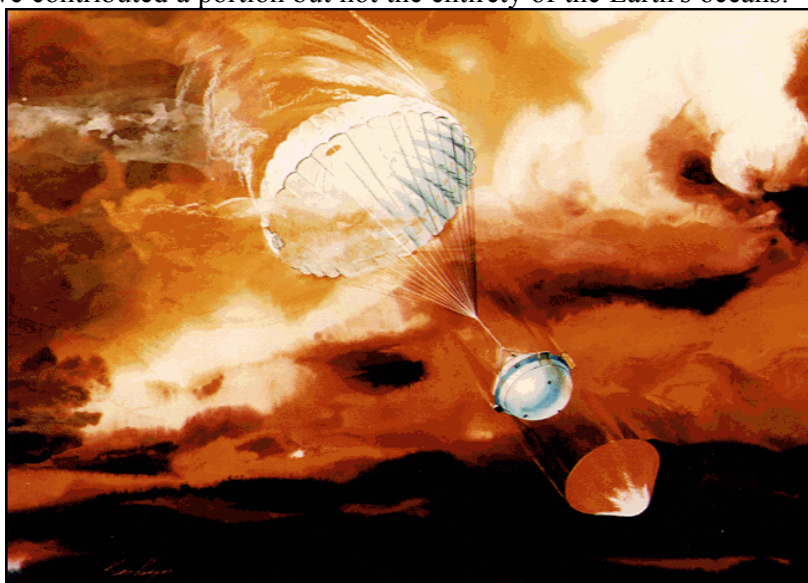


Figure 26. The Galileo Probe employed a parachute as illustrated. The mass spectrometer sampled gas from the

[illegible]

Mahaffy, P. R., T. M. Donahue, S. K. Atreya, T. C. Owen, and H. B. Niemann, 1998: Galileo probe measurements of D/H and $3\text{He}/4\text{He}$ in Jupiter's atmosphere. *Space Sciences Reviews* 84, 251-263, and in the ISSI volume *Primordial Nuclei and their Galactic Evolution* 84, 251-263 eds. R. von Steiger et al. Kluwer academic Publishers, Dordrecht (1988).

Page 24 of 24